ECCOMAS Congress 2016
VII European Congress on Computational Methods in Applied Sciences and Engineering
M. Papadrakakis, V. Papadopoulos, G. Stefanou, V. Plevris (eds.)
Crete Island, Greece, 5–10 June 2016

DETERMINATION OF MESOSCALE RANDOM FIELDS FOR THE APPARENT PROPERTIES OF SPATIALLY RANDOM COMPOSITES

Dimitrios Savvas[1], **George Stefanou**[2]

[1]School of Civil Engineering, National Technical University of Athens
15780 Athens, Greece
e-mail: dimitriosavvas@yahoo.gr

[2] Department of Civil Engineering, Aristotle University of Thessaloniki
54124 Thessaloniki, Greece
e-mail: gstefanou@civil.auth.gr

Keywords: Random Composites, Apparent Properties, Mesoscale random fields, RVE size, XFEM, Monte Carlo Simulation.

Abstract. *The macroscopic mechanical and physical properties of heterogeneous materials can be efficiently determined using either analytical or numerical homogenization techniques where the identification of a representative volume element (RVE) is required over which a fine-scale boundary value problem is solved. In this work, an efficient computational scheme is proposed for the determination of mesoscale random fields for the apparent properties and of the RVE size of particle-reinforced composites based on computer-simulated images of their microstructure. A variable number of microstructure models are directly constructed by segmentation of the composite material image into windows of certain size. The proposed numerical procedure takes into account the particle volume fraction variation through digital image processing of the microstructure models. The proposed approach couples the extended finite element method (XFEM) with Monte Carlo simulation in order to analyze the microstructure models and obtain statistical information (probability distribution, correlation structure) for the apparent properties of the composite in each window size. The XFEM analysis of the microstructure models also leads to upper and lower bounds for their constitutive behavior by solving Dirichlet and Neumann boundary value problems. The RVE is attained within a prescribed tolerance by examining the convergence of these two bounds with respect to the mesoscale size and useful conclusions are derived about the effect of matrix/inclusion stiffness ratio as well as of inclusion volume fraction on the apparent properties and on the RVE size.*

1 INTRODUCTION

The key issue in homogenization methods is the linking of micromechanical characteristics with the random variation of material properties at the macroscale [1, 2, 3, 4]. This link can be established using the Hill-Mandel macro-homogeneity condition [5] among other asymptotic or heterogeneous multiscale methods [6, 7]. In all these methods, the identification of a representative volume element (RVE) of the heterogeneous material is required over which a fine-scale boundary value problem is solved. Then effective material properties can be calculated using the link between the fine and coarse scale equations.

While the concept of unit cell is valid whenever periodicity of microstructure is present, in the case of spatial randomness (e.g. random position, shape, size of inclusions), the identification of RVE must be based on computational convergence schemes with respect to specific apparent properties. The typical procedure consists in setting multiple realizations of the microstructure followed by finite element simulation and statistical analysis of the results [8, 9, 10, 11, 12, 13, 14]. In the context of stochastic finite element analysis of composite structures, the RVE size determines the minimum element size that should be used for discretization at the macroscale [15, 16, 17].

Since the volume fraction is one of the primary microstructural features in homogenization problems, the constant volume fraction assumption can lead to inexact effective properties. In this work, a novel computational scheme is proposed for the determination of RVE size for particle-reinforced composites based on computer-simulated images of their microstructure. A variable number of microstructure models are directly constructed from the composite material image using the moving window technique. In this way, the scatter of inclusions for each sample model is not achieved in an arbitrary manner but is an exact geometrical representation of the corresponding window segment of the composite. Moreover, the volume fraction of inclusions is computed through digital image processing of the microstructure models. The proposed numerical procedure takes into account the local volume fraction variation and thus the obtained RVE can lead to more accurate homogenized properties.

This paper couples the extended finite element method (XFEM) with Monte Carlo simulation (MCS) in order to analyze the microstructure models and obtain statistical information for the constitutive properties of the samples in each window size. The number of MCS depends on the moving window technique and is increasing for small window sizes. The implementation of XFEM is particularly suitable for this type of problems since there is no need to generate conforming finite element (FE) meshes at each MCS [18, 19, 20]. The weak discontinuity in the solution due to material interfaces is captured using nodal enrichment functions within the framework of the partition of unity method to augment the FE approximations over a structured mesh [21]. The XFEM analysis of the microstructure models is then used to compute upper and lower bounds for their constitutive behavior by solving multiple boundary value problems under kinematic and static uniform boundary conditions [22]. The RVE is attained within a prescribed tolerance by examining the convergence of these two bounds with respect to the mesoscale size. Mesoscale random fields describing the spatial variation of the components of the apparent elasticity tensor are also determined.

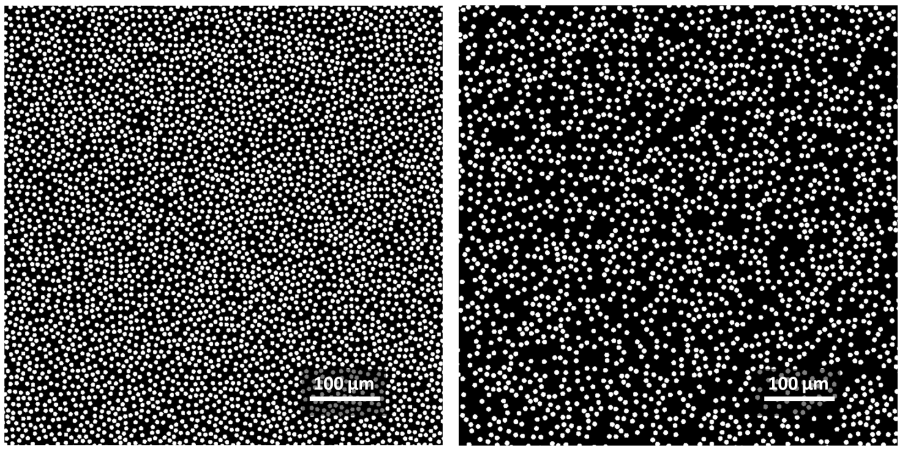

(a) (b)

Figure 1: Computer-simulated images of composite materials containing circular inclusions with a) vf=40% (image 1) and b) vf=20% (image 2).

2 COMPUTATION OF LOCAL VOLUME FRACTION VARIATION

The variability of local volume fraction (vf) in computer-simulated composites is studied in this section exploiting image analysis techniques available in MATLAB software. Specifically, images of two composites containing an initial amount (vf) of 40% and 20% of inclusions, respectively, are processed (see Fig. 1). Both images have dimensions $L_{image} \times L_{image}$ ($L_{image} = 640\mu m$) and an approximate analysis of 5800×5800 pixels. The represented composites contain 4096 and 2048 non-overlapping randomly scattered inclusions, respectively. Each inclusion has circular shape with constant area 40 μm^2 which is equivalent to a constant diameter $d \simeq 7.14\ \mu m$.

The computation of the local volume fraction variation is based on the moving window technique. In this method, an initial window of area $L \times L$ is set at a starting point O of the image and then, by moving this window over the image by a vector $\vec{\xi_p} = \xi_{x_p}\vec{e_x} + \xi_{y_p}\vec{e_y}$ a set of windows of the same size can be extracted (see Fig. 2). In this paper, the moving distance step $\Delta\xi$ is assumed to be the same along both directions. This means that $\xi_{x_p} = i\Delta\xi$ and $\xi_{y_p} = j\Delta\xi$, with i, j the number of steps along the x and y directions, respectively. The total number of windows n_w belonging to each set depends on the image size L_{image}, the investigated window size L and the selected moving distance step $\Delta\xi$ as follows:

$$n_w = \left(\frac{L_{image} - L}{\Delta\xi} + 1\right)^2 \tag{1}$$

By choosing $\Delta\xi = L$ with L an integer divisor of L_{image} the whole image is segmented into $n_w = (L_{image}/L)^2$ non-overlapping windows (mesoscale models). Specifically 10 sets containing n_w=4, 16, 25, 64, 100, 256, 400, 1024, 1600, 4096 windows have been generated by choosing $\Delta\xi = L$= 320, 160, 128, 80, 64, 40, 32, 20, 16, 10 μm, respectively.

The vf of inclusions is computed in each window by using image analysis tools. The histograms of the vf corresponding to each set of windows are shown in Fig. 3 for the two images of Fig. 1. As the dispersion of the inclusions within the composite materials is not uniform, it is obvious that there are regions rich or poor in inclusions. This is clearly illustrated in the histograms where a very large variability of vf is observed for the sets containing windows of small size. Thus in the context of homogenization methods, choosing a RVE size for composite ma-

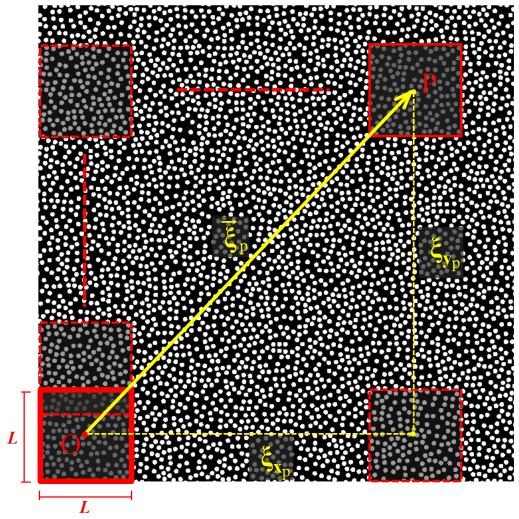

Figure 2: Illustration of the moving window technique.

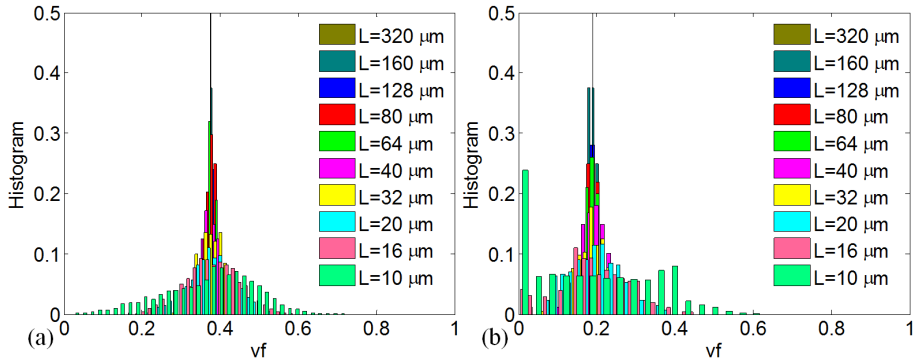

Figure 3: Histograms of vf for various window sizes L for a) image 1, b) image 2.

terials with spatial randomness without considering local vf variability, can lead to unrealistic estimations of their mechanical behavior [23].

3 COMPUTATIONAL PROCEDURE FOR RVE DETERMINATION

According to [24] the homogenization process is based on the fundamental assumption of statistical homogeneity of the heterogeneous medium. This means that all statistical properties of the state variables are the same at any material point and thus a RVE can be identified. While in case of composites with periodic or nearly periodic geometry the RVE is explicitly defined, in case of spatial randomness, the existence of RVE has to be sought using computational methods. In this paper, identification of RVE is performed using a computational procedure based on Hill's definition [5] which postulates separation of scales in the form:

$$d \ll L \ll L_{macro} \tag{2}$$

In the above inequality, the microscale parameter d denotes a characteristic size of the fillers, e.g. their diameter in case of circular inclusions, the mesoscale parameter L denotes the size of the RVE and the macroscale parameter L_{macro} denotes the characteristic length over which the

macroscopic loading varies in space, or in the case of complete scale separation, the size of the macroscopic homogeneous medium.

In the proposed computational procedure, the RVE will be defined with respect to the non-dimensional parameter $\delta = L/d$ with $\delta \in [1, \infty]$. Note that in the absence of spatial periodicity in composite materials the RVE is exactly obtained only in the limit $\delta \to \infty$. However, the RVE can be attained at a finite mesoscale size δ when a particular apparent property derived from statistical volume elements (SVEs) is almost approaching to a constant effective property. At this mesoscale size, the estimation of the particular effective property is not changing with increasing the number of realizations.

In this paper, the RVE is identified in terms of the convergence of the components of the spatially averaged apparent elasticity tensor, which are calculated on mesoscale models of increasing size by applying both kinematic and static uniform boundary conditions. In each investigated mesoscale size δ, variability of vf is taken into account in the computational procedure by processing microstructure models directly extracted from images of the particular composite material (section 2). The RVE obtained from this computational approach is expected to lead to more realistic homogenization results. In the numerical examples of section 4, it will be shown that the convergence rate of the mesoscale models to the RVE is mainly depending on the matrix/inclusion stiffness ratio and volume fraction of the composite material.

3.1 Problem formulation

Let us denote a mesoscale realization of a composite material as $B_\delta(\theta)$ and its boundary surface as $\partial B_\delta(\theta)$, $\theta \in \Theta$ where Θ is the sample space (see Fig. 4). The governing equilibrium equation for the elastostatic problem of the medium is

$$\text{div}\boldsymbol{\sigma}(\theta, \boldsymbol{Y}) + \boldsymbol{b} = 0 \ \text{ in } B_\delta(\theta) \tag{3}$$

where $\boldsymbol{b}$ are the body forces acting on the medium and $\boldsymbol{Y}$ denotes the coordinate system on the mesoscale model $B_\delta(\theta)$ with the stress and strain fields connected by Hooke's elasticity tensor $C(\theta, \boldsymbol{Y})$

$$\boldsymbol{\sigma}(\theta, \boldsymbol{Y}) = C(\theta, \boldsymbol{Y}) : \boldsymbol{\varepsilon}(\theta, \boldsymbol{Y}) \tag{4}$$

These fields can be expressed as a superposition of means ($\bar{\boldsymbol{\sigma}}$ and $\bar{\boldsymbol{\varepsilon}}$) and of zero-mean fluctuations ($\boldsymbol{\sigma'}$ and $\boldsymbol{\varepsilon'}$) as follows:

$$\boldsymbol{\sigma}(\theta, \boldsymbol{Y}) = \bar{\boldsymbol{\sigma}} + \boldsymbol{\sigma'}(\theta, \boldsymbol{Y}) \quad , \quad \boldsymbol{\varepsilon}(\theta, \boldsymbol{Y}) = \bar{\boldsymbol{\varepsilon}} + \boldsymbol{\varepsilon'}(\theta, \boldsymbol{Y}) \tag{5}$$

The means of stress and strain tensors at some point $\boldsymbol{X}$ of the macro-continuum are computed as volume averages over $B_\delta(\theta)$ in the form [5]:

$$\bar{\boldsymbol{\sigma}}(\boldsymbol{X}) = \frac{1}{V_\delta} \int\limits_{B_\delta(\theta)} \boldsymbol{\sigma}(\theta, \boldsymbol{Y}) \, \mathrm{d}V_\delta, \quad \bar{\boldsymbol{\varepsilon}}(\boldsymbol{X}) = \frac{1}{V_\delta} \int\limits_{B_\delta(\theta)} \boldsymbol{\varepsilon}(\theta, \boldsymbol{Y}) \, \mathrm{d}V_\delta \tag{6}$$

Also the volume average of the strain energy can be calculated as:

$$\bar{U} = \frac{1}{2V_\delta} \int\limits_{B_\delta(\theta)} \boldsymbol{\sigma}(\theta, \boldsymbol{Y}) : \boldsymbol{\varepsilon}(\theta, \boldsymbol{Y}) \, \mathrm{d}V_\delta = \frac{1}{2}\overline{\boldsymbol{\sigma} : \boldsymbol{\varepsilon}} = \frac{1}{2}\bar{\boldsymbol{\sigma}} : \bar{\boldsymbol{\varepsilon}} + \frac{1}{2}\overline{\boldsymbol{\sigma'} : \boldsymbol{\varepsilon'}} \tag{7}$$

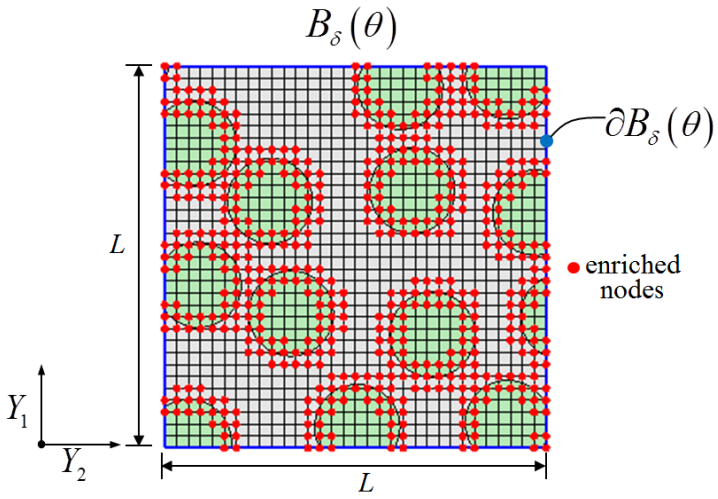

Figure 4: Discretization of a mesoscale model of a spatially random composite material.

Note that for an unbounded space domain $(\delta \to \infty)$ the fluctuation terms in (7) become negligible $\left(\overline{\boldsymbol{\sigma}' : \boldsymbol{\varepsilon}'} = 0\right)$ and thus the following equation holds:

$$\overline{\boldsymbol{\sigma} : \boldsymbol{\varepsilon}} = \bar{\boldsymbol{\sigma}} : \bar{\boldsymbol{\varepsilon}} \tag{8}$$

which is known as Hill's condition. However, at a finite mesoscale, Hill's condition is valid provided that the following constraint is satisfied [25]:

$$\int_{\partial B_\delta} (t - \bar{\boldsymbol{\sigma}} \cdot n) \cdot (u - \bar{\boldsymbol{\varepsilon}} \cdot \boldsymbol{Y}) \, \mathrm{d}S = 0 \tag{9}$$

The constraint equation (9) is a priori satisfied by the following types of boundary conditions:

1. Uniform strains (kinematic, essential or Dirichlet):

$$u(\boldsymbol{Y}) = \bar{\boldsymbol{\varepsilon}} \cdot \boldsymbol{Y} \ , \ \forall \, \boldsymbol{Y} \in \partial B_\delta \tag{10}$$

2. Uniform stresses (static, natural or Neumann):

$$t(\boldsymbol{Y}) = \bar{\boldsymbol{\sigma}} \cdot n \ , \ \forall \, \boldsymbol{Y} \in \partial B_\delta \tag{11}$$

3. Uniform orthogonal-mixed:

$$(t(\boldsymbol{Y}) - \bar{\boldsymbol{\sigma}} \cdot n) \cdot (u(\boldsymbol{Y}) - \bar{\boldsymbol{\varepsilon}} \cdot \boldsymbol{Y}) \ , \ \forall \, \boldsymbol{Y} \in \partial B_\delta \tag{12}$$

4. Periodic:

$$\begin{gathered} u\left(\boldsymbol{Y}^+\right) - u\left(\boldsymbol{Y}^-\right) = \bar{\boldsymbol{\varepsilon}} \cdot \left(\boldsymbol{Y}^+ - \boldsymbol{Y}^-\right) \text{ and } t\left(\boldsymbol{Y}^+\right) + t\left(\boldsymbol{Y}^-\right) = 0 \ , \\ \forall \, \boldsymbol{Y}^+ \in \partial B_\delta^+ \text{ and } \forall \, \boldsymbol{Y}^- \in \partial B_\delta^- \text{ with } \partial B_\delta = \partial B_\delta^+ \cup \partial B_\delta^- \end{gathered} \tag{13}$$

3.2 Computation of apparent properties on mesoscale

Miehe and Koch [22] proposed a computational procedure to define apparent properties (homogenized stresses and overall tangent moduli) of microstructures undergoing small strains. They have shown that apparent properties can be defined in terms of discrete forces and stiffness properties on the boundary of discretized microstructures. Using these deformation-driven algorithms, the apparent stiffness or compliance tensor of a mesoscale model of size δ can be calculated by solving a uniform strain or a uniform stress boundary value problem, respectively. The extended finite element method (XFEM) is used to model the microstructural problems. In the context of XFEM, weak discontinuities (material interfaces) can be captured by a discontinuous approximation of the displacement function $u^h(\boldsymbol{Y})$ as follows [26]:

$$u^h(\boldsymbol{Y}) = \sum_{i \in I} N_i(\boldsymbol{Y})\, u_i + \sum_{j \in J} N_j(\boldsymbol{Y}) \left(\sum_{k=1}^{n_0} \psi_k(\boldsymbol{Y})\, \alpha_{jk} \right) \tag{14}$$

where N are the shape functions of the elements used, I is the set of all nodes in the mesh, J is the set of nodes (denoted as red circles in Fig. 4) that are enriched with the enrichment functions ψ_k, u_i are the classical dofs, α_{jk} are the enriched dofs corresponding to node j whose support is cut by the k^{th} inclusion. To improve the accuracy and convergence of XFEM solution the following enrichment function is used [18]:

$$\psi_k(\boldsymbol{Y}) = \sum_{i \in I} N_i(\boldsymbol{Y}) \left| \phi_i^k \right| - \left| \sum_{i \in I} N_i(\boldsymbol{Y})\, \phi_i^k \right| \tag{15}$$

with ϕ_i^k the nodal values of the level set function corresponding to the k^{th} circular inclusion. The adopted computational procedure is outlined below for the two cases of uniform boundary conditions. More details can be found in [27].

3.2.1 Uniform strains

A prescribed uniform strain tensor $\bar{\boldsymbol{\varepsilon}} = [\bar{\varepsilon}_{11} \;\; \bar{\varepsilon}_{22} \;\; 2\bar{\varepsilon}_{12}]^T$ is applied on the boundary ∂B_δ of a discretized mesoscale model, as that of Fig. 4 through displacement boundary conditions (Dirichlet) in the form:

$$u_b = D_b^T \bar{\boldsymbol{\varepsilon}} \tag{16}$$

where D_b is a geometric matrix which depends on the coordinates of the boundary node b and is defined as:

$$D_b = \frac{1}{2} \begin{bmatrix} 2Y_1 & 0 \\ 0 & 2Y_2 \\ Y_2 & Y_1 \end{bmatrix} \quad \text{with} \quad (Y_1, Y_2) \in \boldsymbol{Y} \tag{17}$$

The static problem is denoted by:

$$\begin{bmatrix} K_{ii} & K_{ib} \\ K_{bi} & K_{bb} \end{bmatrix} \begin{bmatrix} U_i \\ U_b \end{bmatrix} = \begin{bmatrix} F_i \\ F_b \end{bmatrix} \tag{18}$$

where the subscripts i and b denote internal and boundary nodes, respectively. Then the apparent stiffness tensor $C_\delta^D(\theta)$ of the mesoscale model of size δ under Dirichlet boundary conditions

can be calculated in terms of the condensed stiffness matrix $\tilde{K}_{bb} = K_{bb} - K_{bi}K_{ii}^{-1}K_{ib}$ in the form:

$$C_{\delta}^{D}(\theta) = \frac{1}{V_{\delta}}\mathbb{D}\tilde{K}_{bb}\mathbb{D}^{T} \tag{19}$$

with $\mathbb{D} = [D_1\ D_2\ ...\ D_M]$, M the total number of boundary nodes.

3.2.2 Uniform stresses

A prescribed uniform stress tensor $\bar{\boldsymbol{\sigma}} = [\bar{\sigma}_{11}\ \ \bar{\sigma}_{22}\ \ 2\bar{\sigma}_{12}]^{T}$ is applied on the boundary surface ∂B_{δ} of a discretized mesoscale model, as that of Fig. 4 through traction boundary conditions (Neumann) as follows:

$$F_b = S_b^{T}\bar{\boldsymbol{\sigma}} \tag{20}$$

where S_b is a matrix depending on the components of the discrete area vector $\mathbf{a}_b$ which is given in terms of the nodal coordinates of the neighboring boundary nodes $b-1$, b and $b+1$ in the form:

$$\mathbf{a}_b = \frac{1}{2}\left[\boldsymbol{Y_{b+1}} - \boldsymbol{Y_{b-1}}\right] \times \boldsymbol{e_n} \tag{21}$$

These nodes are oriented so that the cross product with the Cartesian, out-of-plane, base vector $\boldsymbol{e_n}$ yields $\mathbf{a}_b$ as an outward normal vector at the boundary node b. Thus the matrix S_b is defined as:

$$S_b = \begin{bmatrix} \mathrm{a}_{b_1} & 0 \\ 0 & \mathrm{a}_{b_2} \\ \mathrm{a}_{b_2} & \mathrm{a}_{b_1} \end{bmatrix} \tag{22}$$

Then the apparent compliance tensor $S_{\delta}^{N}(\theta)$ of the mesoscale model of size δ under Neumann boundary conditions can be calculated in terms of the condensed stiffness matrix $\tilde{K}_{bb}$ in the form:

$$S_{\delta}^{N}(\theta) = \frac{1}{V_{\delta}}\mathbb{S}\tilde{K}_{bb}^{-1}\mathbb{S}^{T} \tag{23}$$

where $\mathbb{S} = [S_1\ S_2\ ...\ S_M]$ with M the total number of boundary nodes. For this type of boundary conditions the apparent stiffness tensor is obtained by inverting the compliance tensor of Eq. (23):

$$C_{\delta}^{N}(\theta) = \left[S_{\delta}^{N}(\theta)\right]^{-1} \tag{24}$$

Dirichlet and Neumann boundary conditions provide upper and lower bounds of the strain energy which converge to each other as the mesoscale size δ is increasing. Thus the following relation holds [28]:

$$\left\{\begin{array}{ll} \frac{1}{2}\left[\bar{\boldsymbol{\varepsilon}} : C_{\delta}^{N}(\theta) : \bar{\boldsymbol{\varepsilon}}\right] < \frac{1}{2}\left[\bar{\boldsymbol{\varepsilon}} : C_{\delta}^{D}(\theta) : \bar{\boldsymbol{\varepsilon}}\right] & \text{for } \delta \text{ finite} \\ \frac{1}{2}\left[\bar{\boldsymbol{\varepsilon}} : C_{\infty}^{N}(\theta) : \bar{\boldsymbol{\varepsilon}}\right] = \frac{1}{2}\left[\bar{\boldsymbol{\varepsilon}} : C_{\infty}^{D}(\theta) : \bar{\boldsymbol{\varepsilon}}\right] & \text{for } \delta \to \infty \end{array}\right\} \tag{25}$$

In case of uniaxial strains $\bar{\boldsymbol{\varepsilon}} = \left([1 \;\; 0 \;\; 0]^T \text{ or } [0 \;\; 1 \;\; 0]^T \right)$ or simple shear $\bar{\boldsymbol{\varepsilon}} = [0 \;\; 0 \;\; 1]^T$ the following notation can be used:

$$C_\delta^N(\theta) \leq C_\delta^D(\theta) \tag{26}$$

4 RESULTS AND DISCUSSION

In this section, the spatial average (mean) of the apparent moduli is calculated at each size δ from n_w mesoscale models extracted by using the window technique on the composite images of section 2. Thus the following formula for the mean is used:

$$\overline{C_\delta(\theta)} = \frac{1}{n_w} \sum_{p=1}^{n_w} C_\delta\left(\vec{\xi}_p, \theta\right) \tag{27}$$

with $\vec{\xi}_p$ the position vector of the p-th mesoscale window model on the image (see Fig. 2). Following the notation of Eq. (26) the bounds $\overline{C_\delta^N(\theta)}$ and $\overline{C_\delta^D(\theta)}$ are calculated for the axial and shear components of the apparent elasticity tensor. Note that, while the constituent materials of the composite are considered isotropic, the computational method of section 3.2 results in an anisotropic apparent elasticity tensor due to spatial randomness. Composites containing either stiff or compliant inclusions are investigated which are obtained by keeping the Young's modulus of the matrix constant at $E_m = 1$ GPa and varying the Young's modulus of the inclusions E_{in}. The Poisson ratio is assumed to be the same for the two phases, $\nu_m = \nu_{in} = 0.3$. All components of the apparent elasticity tensor computed in this section are in GPa.

4.1 Effect of volume fraction and stiffness ratio on RVE size

The convergence of $\overline{C_\delta^N(\theta)}$ and $\overline{C_\delta^D(\theta)}$ with respect to the non-dimensional parameter δ is illustrated in Fig. 5 for the composite materials of images 1 and 2 (see Fig. 1). The results refer to the average axial stiffness $C_{ii}/2$ $(i = 1, 2)$ and shear stiffness $C_{33} \equiv G$ components of the mean elasticity tensor. As mentioned before in section 2, image 1 corresponds to a composite with initial vf=40%, whereas image 2 corresponds to a composite with initial vf=20%. Note that both composites contain circular inclusions of constant size ($d \simeq 7.14\ \mu m$). The effect of volume fraction on the mechanical properties of the composite is also illustrated in Fig. 5. It can be observed that the convergence rate of the two numerical bounds with respect to δ is slower as vf increases. This means that, in order to perform homogenization in composites with high volume fraction, a much larger RVE has to be used.

The results of a parametric study with respect to matrix/inclusion stiffness ratio are shown in Figs. 6 and 7 for the composite of image 1. The cases of stiff (E_{in}/E_m=10, 100, 1000) and compliant (E_{in}/E_m=0.1, 0.01, 0.001) inclusions have been tested. As the Young's modulus of the inclusions increases, the computed apparent properties of the composite increase as well. The effect of stiffness ratio on the convergence rate of the apparent properties is also illustrated in these figures. This effect is better illustrated in Fig. 8 where the discrepancy (tolerance) e_δ between the numerical bounds is plotted against the non-dimensional parameter δ for both composites examined (images 1 and 2). The discrepancy is calculated as:

$$e_\delta = \left| \frac{\overline{C_{ij}^D} - \overline{C_{ij}^N}}{\overline{C_{ij}^D}} \right|_\delta \tag{28}$$

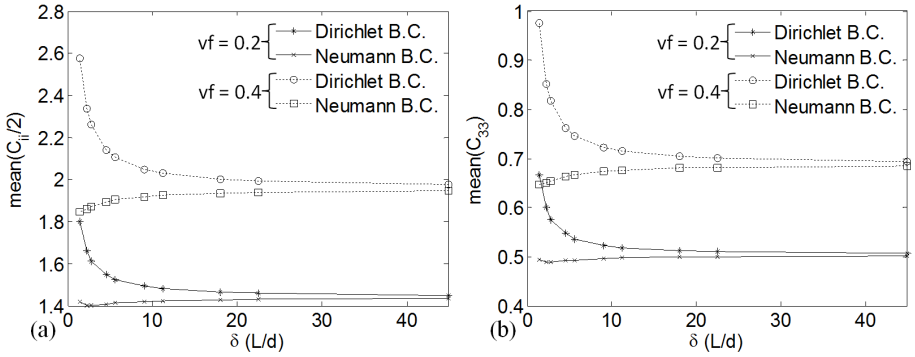

Figure 5: Comparison of numerical bounds of apparent properties for the composites of images 1 and 2 containing stiff inclusions ($E_{in}/E_m = 10$).

where $\overline{C_{ij}^D}$ and $\overline{C_{ij}^N}$ are the components of the spatially averaged apparent elasticity tensor obtained by applying Dirichlet and Neumann boundary conditions, respectively.

4.2 Determination of mesoscale random fields

In this section, random fields for the volume fraction and the apparent elasticity tensor of the composite of image 1 (see section 2) are obtained in mesoscale sizes δ from the simulation of a large number of SVE models extracted using the moving window technique. In order to obtain accurate statistical properties, the moving distance step of the method has been chosen as $\Delta\xi = 0.25L$, with L the moving window size. Specifically, random fields for δ =5.605, 11.210 and 22.420 have been derived by simulating n_w =3721, 841 and 169 SVEs, respectively (see Eq. (1) in section 2 for n_w). All the presented results refer to kinematic uniform boundary conditions.

Figs. 9 and 10 depict the computed random fields along with the respective empirical distributions and 2-D spatial correlations of the average axial and shear components of the apparent elasticity tensor, for the three mesoscale sizes δ examined. Note that the spatial correlations ρ_A^B have been calculated for every lag $(\xi_x,\ \xi_y)$ according to the following formula:

$$\rho_A^B\left(\xi_x,\ \xi_y\right) = \frac{1}{n_w - 1}\sum_{i=0}^{\sqrt{n_w}}\sum_{j=0}^{\sqrt{n_w}}\left(\frac{A\left(x_i,\ y_j\right) - \bar{A}}{\sigma_A}\right)\left(\frac{B\left(x_i + \xi_x,\ y_j + \xi_y\right) - \bar{B}}{\sigma_B}\right) \tag{29}$$

$$-\sqrt{n_w}\Delta\xi \leq \xi_x \leq \sqrt{n_w}\Delta\xi\ ,\ -\sqrt{n_w}\Delta\xi \leq \xi_y \leq \sqrt{n_w}\Delta\xi$$

with ρ_A^B denoting auto-correlations when quantity $A \equiv B$, otherwise cross-correlations are defined. $\bar{A}$, $\bar{B}$ are the spatial average values while σ_A, σ_B are the standard deviations of quantities A, B, respectively. The mesoscale random fields of the components of the apparent elasticity tensor in Figs. 9 and 10 have been derived for stiffness ratio $E_{in}/E_m = 10$. A general observation for all mesoscale random fields is that their empirical PDFs become narrower as the mesoscale size δ increases. In other words, the random field tends to a random variable and thus the SVE tends to the RVE as δ increases. The auto-correlations for lag $(\xi_x = 0,\ \xi_y = 0)$ are 1 and tend to zero for lag values $|\xi_x| > L$ and $|\xi_y| > L$.

The 1-D cross correlations $\rho_{\nu f}^{0.5(C_{11}+C_{22})}$ and $\rho_{\nu f}^{C_{33}}$ are depicted in Figs. 11 and 12, respectively, for lag values along x $(\xi_x,\ \xi_y = 0)$ and y $(\xi_x = 0,\ \xi_y)$ for stiffness ratio E_{in}/E_m =10 and 1000.

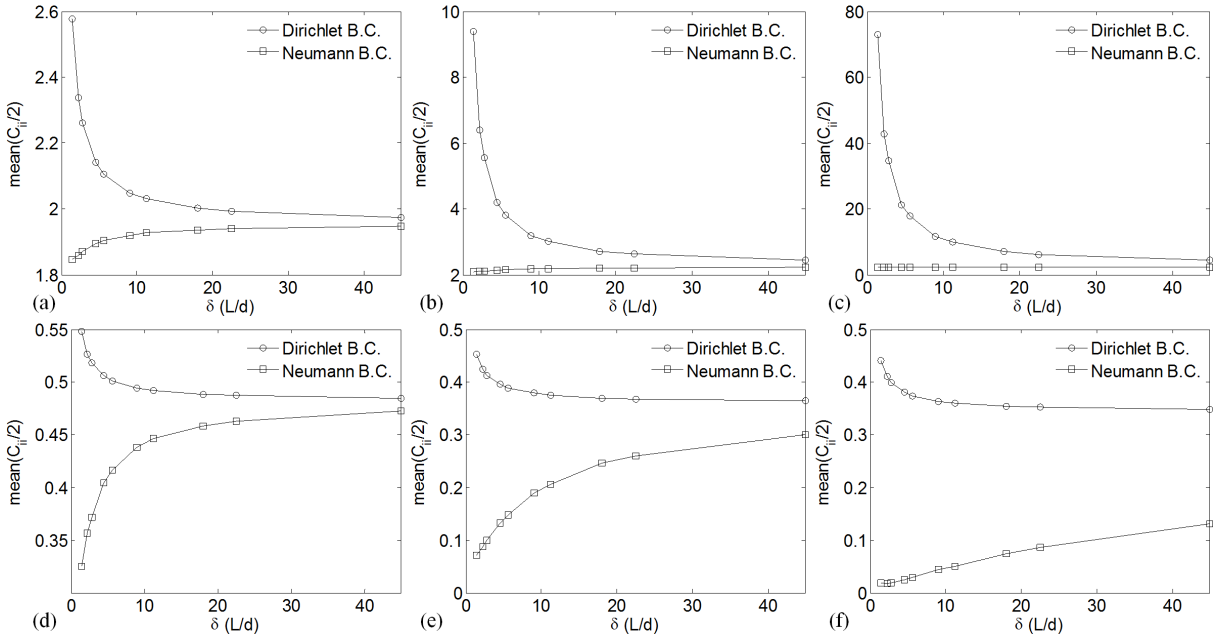

Figure 6: Convergence of numerical bounds on the average axial stiffness ($C_{ii}/2$) with respect to mesoscale size δ for stiffness ratio a) $E_{in}/E_m = 10$, b) $E_{in}/E_m = 100$, c) $E_{in}/E_m = 1000$, d) $E_{in}/E_m = 0.1$, e) $E_{in}/E_m = 0.01$, f) $E_{in}/E_m = 0.001$.

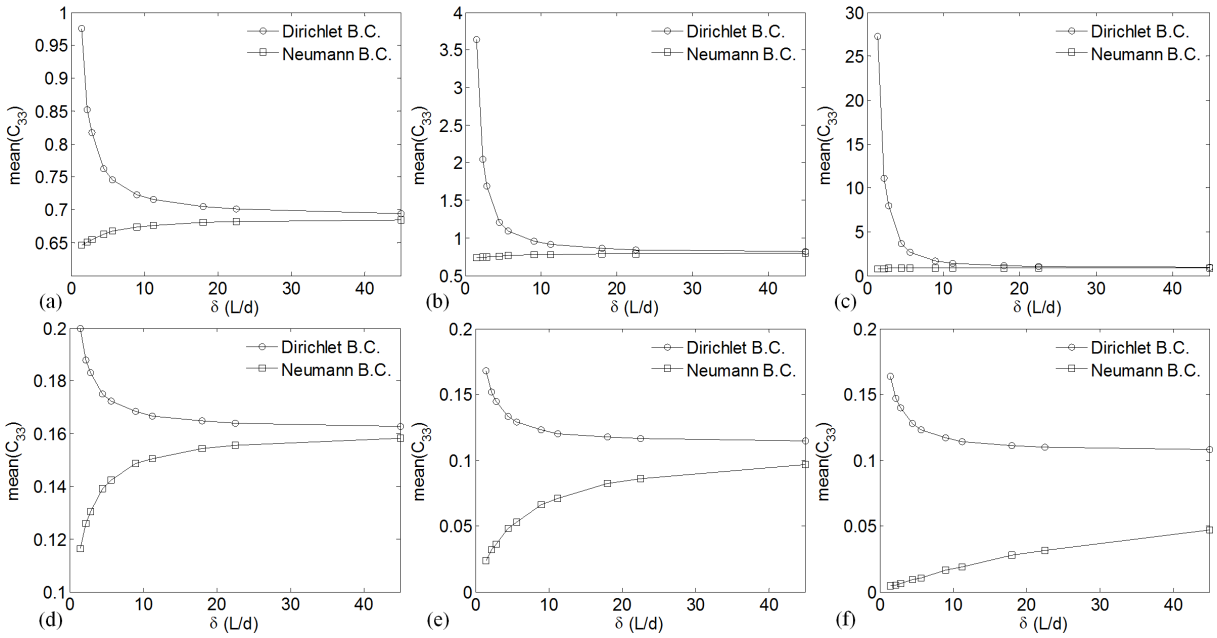

Figure 7: Convergence of numerical bounds on the shear stiffness (C_{33}) with respect to mesoscale size δ for stiffness ratio a) $E_{in}/E_m = 10$, b) $E_{in}/E_m = 100$, c) $E_{in}/E_m = 1000$, d) $E_{in}/E_m = 0.1$, e) $E_{in}/E_m = 0.01$, f) $E_{in}/E_m = 0.001$.

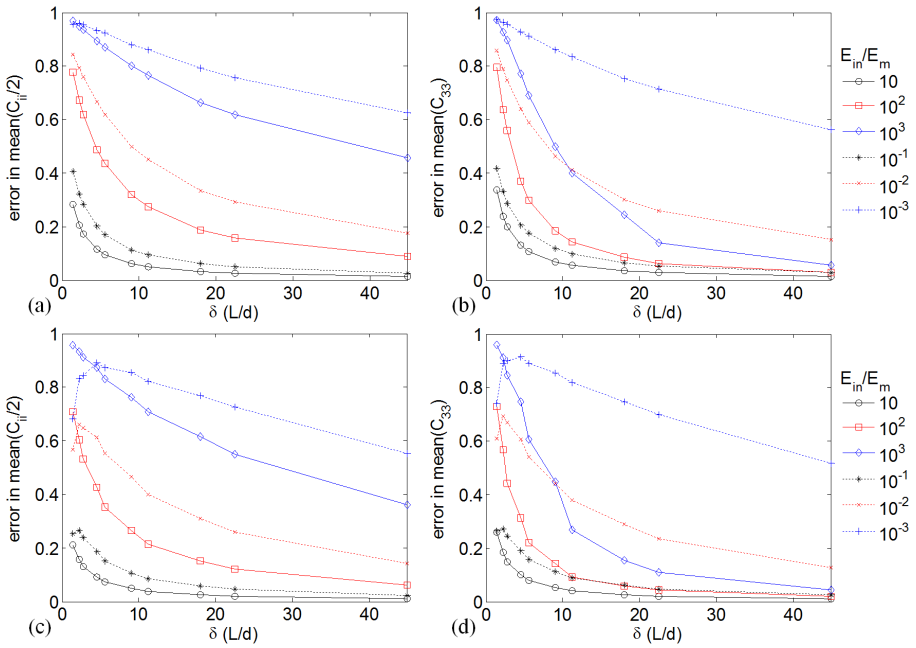

Figure 8: Discrepancy between upper and lower bounds with respect to mesoscale size δ for the composites of image 1 (a-b) and image 2 (c-d) and various cases of stiffness ratio.

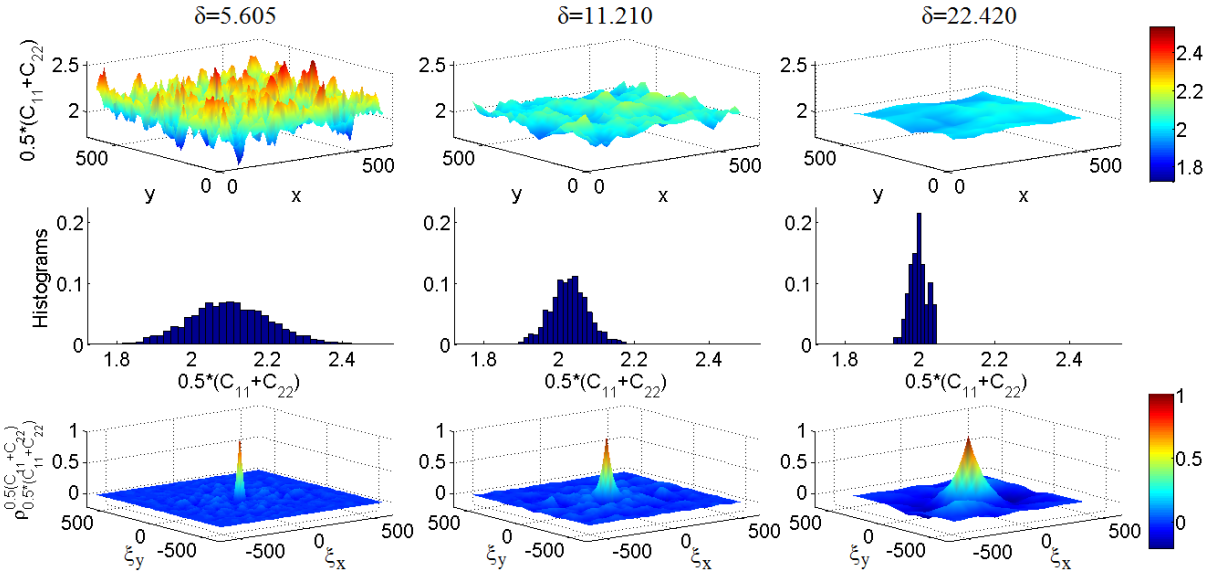

Figure 9: Mesoscale random fields for average axial stiffness ($E_{in}/E_m = 10$).

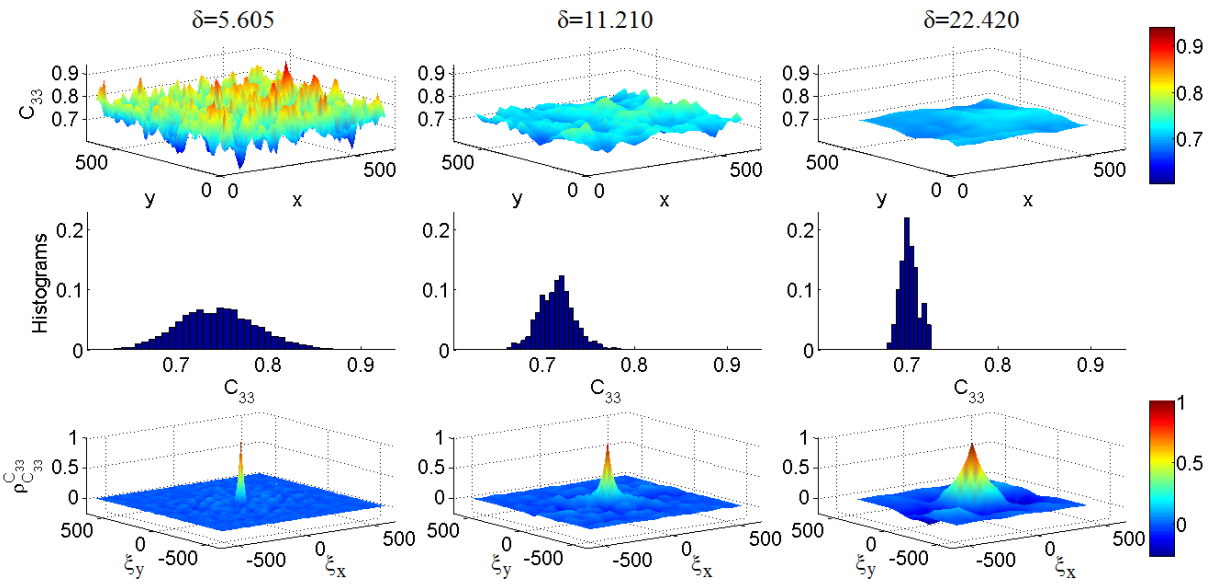

Figure 10: Mesoscale random fields for shear stiffness ($E_{in}/E_m = 10$).

All cross-correlations are between -1 and +1 and tend to zero for $|\xi_x| > L$ or $|\xi_y| > L$. This can be attributed to the fact that the probability of SVE models sharing common inclusions decreases as the length of the vector $\vec{\xi}_p$ (see Fig. 2) increases. A decrease on the values of cross-correlations with the increase of stiffness ratio is also observed, as in [29], especially for $|\xi_x| \leq L$ and $|\xi_y| \leq L$ for all sizes δ. This could be an explanation of the fact that the RVE size can not be defined within a reasonable tolerance for the case of high stiffness ratio (see results of section 4.1). More information about the statistical characteristics of mesoscale random fields is provided in [27].

5 CONCLUSIONS

In this paper, a novel computational procedure based on XFEM and MCS has been proposed for the determination of mesoscale random fields for the apparent properties and of the RVE size of spatially random composites. The proposed approach takes into account the local volume fraction variation by processing computer-simulated images of composites with randomly dispersed inclusions. A variable number of microstructure models were derived directly from the images using the moving window technique. The XFEM analysis of the microstructure models was used to compute upper and lower bounds on the apparent material properties by solving multiple boundary value problems under kinematic and static uniform boundary conditions. The RVE was attained within a prescribed tolerance by examining the convergence of these two bounds with respect to the mesoscale size. The effect of matrix/inclusion stiffness ratio as well as of the volume fraction of inclusions on the RVE size was highlighted. The proposed computational procedure can provide with a more realistic RVE because it incorporates the local volume fraction variation present in real composites and can be extended to any filler-reinforced composite as it is based on image analysis of computer-simulated microstructures. Finally, the obtained results can be used in the framework of homogenization methods and stochastic finite element analysis of composite structures.

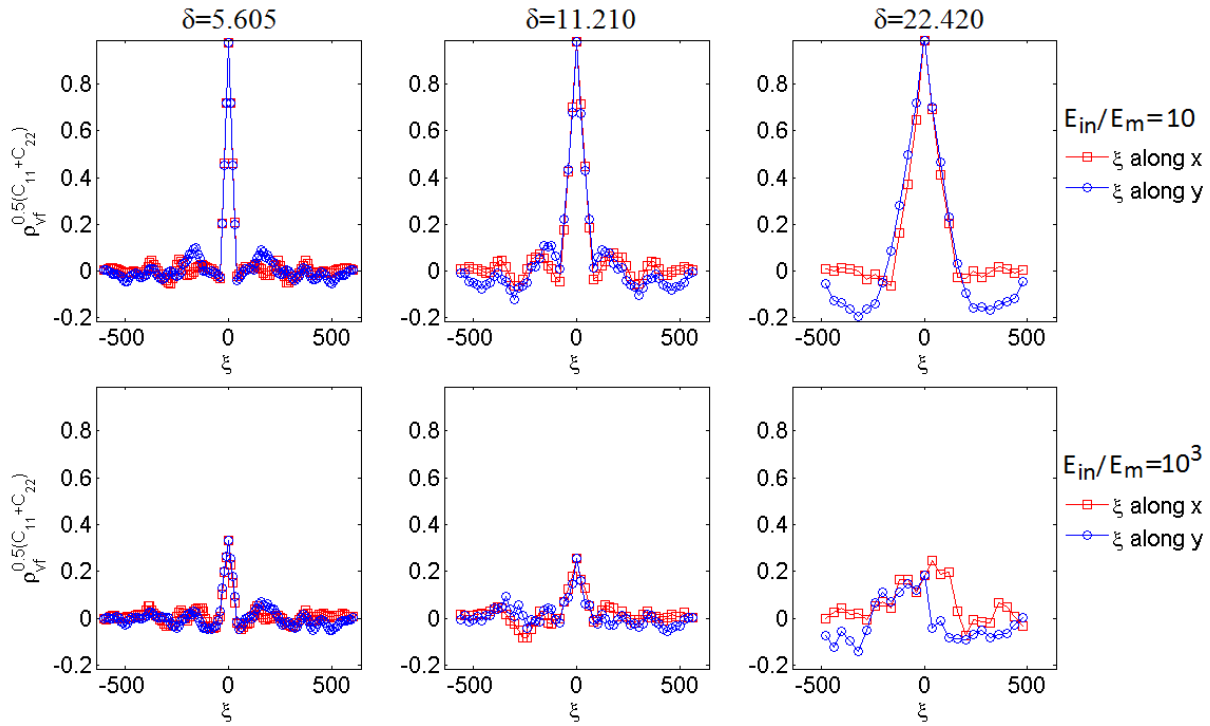

Figure 11: Cross correlations at $(\xi_x,\ \xi_y = 0)$ and $(\xi_x = 0,\ \xi_y)$ for $E_{in}/E_m = 10$ and $E_{in}/E_m = 1000$.

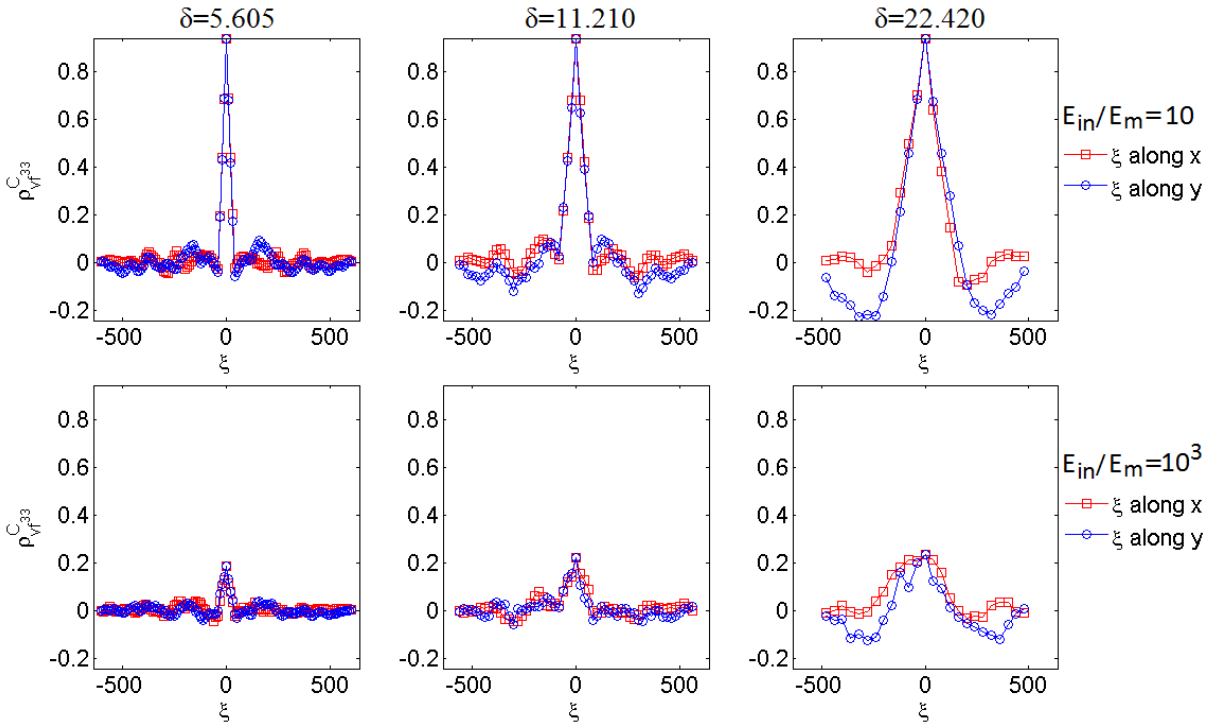

Figure 12: Cross correlations at $(\xi_x,\ \xi_y = 0)$ and $(\xi_x = 0,\ \xi_y)$ for $E_{in}/E_m = 10$ and $E_{in}/E_m = 1000$.

ACKNOWLEDGEMENTS

The financial support provided by the European Research Council Advanced Grant "MASTER - Mastering the computational challenges in numerical modeling and optimum design of CNT reinforced composites" (ERC-2011-ADG 20110209) is gratefully acknowledged by the authors.

REFERENCES

[1] S. Baxter and L. Graham, "Characterization of random composites using moving-window technique," *Journal of Engineering Mechanics*, vol. 126, no. 4, pp. 389–397, 2000.

[2] X. F. Xu and L. Graham-Brady, "A stochastic computational method for evaluation of global and local behavior of random elastic media," *Computer Methods in Applied Mechanics and Engineering*, vol. 194, no. 42, pp. 4362–4385, 2005.

[3] D. Charmpis, G. Schuëller, and M. Pellissetti, "The need for linking micromechanics of materials with stochastic finite elements: A challenge for materials science," *Computational Materials Science*, vol. 41, no. 1, pp. 27–37, 2007.

[4] A. Clément, C. Soize, and J. Yvonnet, "Uncertainty quantification in computational stochastic multiscale analysis of nonlinear elastic materials," *Computer Methods in Applied Mechanics and Engineering*, vol. 254, pp. 61–82, 2013.

[5] R. Hill, "Elastic properties of reinforced solids: some theoretical principles," *Journal of the Mechanics and Physics of Solids*, vol. 11, no. 5, pp. 357–372, 1963.

[6] A. Bensoussan, J.-L. Lions, and G. Papanicolaou, *Asymptotic analysis for periodic structures*, vol. 374. American Mathematical Soc., 2011.

[7] W. E, B. Engquist, X. Li, W. Ren, and E. Vanden-Eijnden, "Heterogeneous multiscale methods: a review," *Commun. Comput. Phys*, vol. 2, no. 3, pp. 367–450, 2007.

[8] T. Kanit, S. Forest, I. Galliet, V. Mounoury, and D. Jeulin, "Determination of the size of the representative volume element for random composites: statistical and numerical approach," *International Journal of solids and structures*, vol. 40, no. 13, pp. 3647–3679, 2003.

[9] M. Ostoja-Starzewski, "Material spatial randomness: From statistical to representative volume element," *Probabilistic engineering mechanics*, vol. 21, no. 2, pp. 112–132, 2006.

[10] X. F. Xu and X. Chen, "Stochastic homogenization of random elastic multi-phase composites and size quantification of representative volume element," *Mechanics of Materials*, vol. 41, no. 2, pp. 174–186, 2009.

[11] M. Silani, H. Talebi, S. Ziaei-Rad, P. Kerfriden, S. P. Bordas, and T. Rabczuk, "Stochastic modelling of clay/epoxy nanocomposites," *Composite Structures*, vol. 118, pp. 241–249, 2014.

[12] J. Ma, J. Zhang, L. Li, P. Wriggers, and S. Sahraee, "Random homogenization analysis for heterogeneous materials with full randomness and correlation in microstructure based on finite element method and monte-carlo method," *Computational Mechanics*, vol. 54, no. 6, pp. 1395–1414, 2014.

[13] J. Zeman and M. Sejnoha, "From random microstructures to representative volume elements," *Modelling and Simulation in Materials Science and Engineering*, vol. 15, no. 4, pp. 325–335, 2007.

[14] J. Wimmer, B. Stier, J.-W. Simon, and S. Reese, "Computational homogenisation from a 3d finite element model of asphalt concrete–linear elastic computations," *Finite Elements in Analysis and Design*, vol. 110, pp. 43–57, 2016.

[15] M. Ostoja-Starzewski and X. Wang, "Stochastic finite elements as a bridge between random material microstructure and global response," *Computer Methods in Applied Mechanics and Engineering*, vol. 168, no. 1, pp. 35–49, 1999.

[16] V. Lucas, J.-C. Golinval, S. Paquay, V.-D. Nguyen, L. Noels, and L. Wu, "A stochastic computational multiscale approach; application to mems resonators," *Computer Methods in Applied Mechanics and Engineering*, vol. 294, pp. 141–167, 2015.

[17] G. Stefanou, D. Savvas, and M. Papadrakakis, "Stochastic finite element analysis of composite structures based on material microstructure," *Composite Structures*, vol. 132, pp. 384–392, 2015.

[18] N. Moës, M. Cloirec, P. Cartraud, and J.-F. Remacle, "A computational approach to handle complex microstructure geometries," *Computer Methods in Applied Mechanics and Engineering*, vol. 192, no. 28, pp. 3163–3177, 2003.

[19] B. Hiriyur, H. Waisman, and G. Deodatis, "Uncertainty quantification in homogenization of heterogeneous microstructures modeled by XFEM," *International Journal for Numerical Methods in Engineering*, vol. 88, no. 3, pp. 257–278, 2011.

[20] D. Savvas, G. Stefanou, M. Papadrakakis, and G. Deodatis, "Homogenization of random heterogeneous media with inclusions of arbitrary shape modeled by XFEM," *Computational Mechanics*, vol. 54, no. 5, pp. 1221–1235, 2014.

[21] J. M. Melenk and I. Babuška, "The partition of unity finite element method: basic theory and applications," *Computer Methods in Applied Mechanics and Engineering*, vol. 139, no. 1, pp. 289–314, 1996.

[22] C. Miehe and A. Koch, "Computational micro-to-macro transitions of discretized microstructures undergoing small strains," *Archive of Applied Mechanics*, vol. 72, no. 4-5, pp. 300–317, 2002.

[23] S. H. R. Sanei and R. S. Fertig, "Uncorrelated volume element for stochastic modeling of microstructures based on local fiber volume fraction variation," *Composites Science and Technology*, vol. 117, pp. 191–198, 2015.

[24] Z. Hashin, "Analysis of composite materials: A survey," *Journal of Applied Mechanics*, vol. 50, no. 2, pp. 481–505, 1983.

[25] S. Hazanov and C. Huet, "Order relationships for boundary conditions effect in heterogeneous bodies smaller than the representative volume," *Journal of the Mechanics and Physics of Solids*, vol. 42, no. 12, pp. 1995–2011, 1994.

[26] T. Belytschko, R. Gracie, and G. Ventura, "A review of extended/generalized finite element methods for material modeling," *Modelling and Simulation in Materials Science and Engineering*, vol. 17, no. 4, pp. 1–24, 2009.

[27] D. Savvas, G. Stefanou, and M. Papadrakakis, "Determination of RVE size for random composites with local volume fraction variation," *Computer Methods in Applied Mechanics and Engineering*, in press, 2016.

[28] P. M. Suquet, "Elements of homogenization for inelastic solid mechanics," in *E. Sanchez-Palencia and A. Zaoui, Eds., Homogenization Techniques for Composite Media*, pp. 193–278, Springer, 1987.

[29] M. P. Sena, M. Ostoja-Starzewski, and L. Costa, "Stiffness tensor random fields through upscaling of planar random materials," *Probabilistic Engineering Mechanics*, vol. 34, pp. 131–156, 2013.